Open Ceramics 15 (2023) 100418

Contents lists available at ScienceDirect

Open Ceramics

journal homepage: www.sciencedirect.com/journal/open-ceramics

Dissolution-precipitation synthesis and cold sintering of mussel shells-derived hydroxyapatite and hydroxyapatite/chitosan composites for bone tissue engineering

Anna Galotta [a,*], Kristaps Rubenis [b], Janis Locs [b,c], Vincenzo M. Sglavo [a,d]

[a] Department of Industrial Engineering, University of Trento, Via Sommarive 9, 38123, Trento, Italy
[b] Rudolfs Cimdins Riga Biomaterials Innovations and Development Centre of RTU, Institute of General Chemical Engineering, Faculty of Materials Science and Applied Chemistry, Riga Technical University, Pulka St. 3/3, Riga, LV-1007, Latvia
[c] Baltic Biomaterials Centre of Excellence, Headquarters at Riga Technical University, Riga, Latvia
[d] INSTM, Via G. Giusti 9, 50121, Firenze, Italy

ARTICLE INFO

Keywords:
Dissolution-precipitation synthesis
Cold sintering
Mussel shells
Hydroxyapatite
Shrimp shells
Chitosan
Composite

ABSTRACT

In the present work, seafood by-products and derivates were exploited as raw materials to produce nanocrystalline calcium phosphates-based composites in light of the rising demand for waste recovery and valorisation. Mussel shells were transformed into hydroxyapatite by dissolution-precipitation synthesis at 45 °C, whereas chitosan from shrimp shells was introduced as a reinforcing biopolymer to produce hydroxyapatite/chitosan composites. The synthesised hydroxyapatite and hydroxyapatite/chitosan composite powders were cold sintered at room temperature under 1 GPa pressure for 10 min. The materials were consolidated up to ~90% relative density and characterized mechanically. By increasing the polymer content up to 10 wt%, the flexural strength of the sintered pellets increases from ~45 MPa to ~57 MPa while the hardness decreases from ~1.1 GPa to ~0.8 GPa, thus better addressing the mechanical properties of cortical bone. Furthermore, hydroxyapatite/chitosan composites were proven to be bioactive, this demonstrating their potential use in bone tissue engineering applications.

1. Introduction

Waste recovery and valorisation are fundamental pillars of the green economy [1]. Recently, the concept of a "blue" economy has also been introduced to depict all those strategies aiming at the preservation of marine environment, at a conscious and responsible use of marine resources [2,3], and at the conferment of an added value to discarded marine by-products (seashells (i.e., from oysters, clams, scallops, mussel etc. [4]), crustacean exoskeletons (i.e., from crabs, shrimps etc. [5]), fish bones and scales (i.e., from cuttlefish, sea bream, salmon etc. [6]), meat residuals etc.) [7–10]. Worldwide shellfish aquaculture has been increasing of ~25% between 2009 and 2019 [11], with a consequent abundance of discarded post-consumption shells, often causing environmental pollution due to their confinement in landfills [12,13]. Therefore, shells represent an attractive, easily accessible and low-cost raw material [14]. Seashells recovery has been already investigated in the past decades as a source of fine and coarse aggregates for concrete [15,16], biofilters for soil and wastewater treatments [17–19], heterogeneous catalysts for biodiesel [20,21] and biogenic calcium carbonate for the pharmaceutical industry [22] and the biomedical field [23–25]. In particular, mussel shells-derived calcium carbonate was found to contain traces of Sr, Mg and Na [26–28], which promote cell activities and potentially enhance the biological properties of the resulting bioceramic material [29–33]. Nevertheless, the substitutional ion content can vary, being influenced by seashell source type, origin, geographical location and possible environmental pollution. For example, Lee et al. [26] found in seashells a Sr and Mg content of ~2188 ppm and ~166 ppm, respectively, whereas Macha et al. [27] reported an ion concentration of ~250 ppm for Sr and ~220 ppm for Mg in untreated mussel shells. In the present work, mussel shells and chitosan from shrimp shells are exploited as raw materials to produce calcium phosphate (CaP)--based composites to resemble the composition of natural bone tissue, mostly composed of calcium deficient low-crystalline carbonated hydroxyapatite (~70%), collagen (~20–25%, mostly type I) and water

* Corresponding author.
E-mail address: anna.galotta@unitn.it (A. Galotta).

https://doi.org/10.1016/j.oceram.2023.100418
Received 17 May 2023; Received in revised form 13 July 2023; Accepted 22 July 2023
Available online 28 July 2023

(5–10%) [34]. Chitosan, a natural polysaccharide, has been widely studied for bone tissue engineering applications due its multiplex advantages such as easy functionalization for drug delivery purposes, hydrophilic behaviour, non-harmful degradation by-products, ability to accelerate wound healing and support to adhesion, proliferation and differentiation of mesenchymal stem cells into bone cells [35–38] Nonetheless, chitosan improves the mechanical properties of CaP [39,40] and shows potential antimicrobial properties which could reduce the possibility of bone infections, being one of the main post-surgery drawbacks [41,42]. CaP/chitosan composites were produced by dissolution-precipitations synthesis. Among other methods, dissolution-precipitation is easy to be implemented for one-pot synthesis of ceramic-based composites, ensuring a homogeneous distribution of the filler within the ceramic material, in comparison to simply dry mixing [43,44]. In addition, it allows high control over the reaction throughout the entire process, it guarantees the production of very fine powders in a relatively short time even at low temperature and it is suitable for large scale production [45,46]. Ceramic/polymer composites are usually difficult to be processed in a single step, due to the different processing temperature range. In this scenario, cold sintering is an avant-garde technique that allows to consolidate ceramics and ceramic-based composites at temperature below 350 °C by the simultaneous application of moderate heat and of an external pressure, usually for times shorter than 1 h and in the presence of a transient liquid phase [47–50]. Cold sintering is suitable for consolidating temperature-sensitive ceramics thus avoiding phase transformation and grain growth [51–53]. Cold sintering of hydroxyapatite has been already reported in the literature, but the consolidation was carried out only with the aid of temperature (150–200 °C) [54–57]. In addition, cold sintering of calcium phosphates could also avoid the surface chemical reactivity reduction observed in such materials already after heat treatment of 450 °C, due to the formation of an alkaline layer [58,59]. Such layer affects the response of osteoclasts, especially at the early post-implantation stages, by downregulating their resorption activity [58,59]. Therefore, cold sintering could lead to different biological response of calcium phosphates in comparison to the high temperature-treated CaP.

The present work aimed at transforming seafood waste into future candidate scaffolds for bone tissue engineering by combining dissolution-precipitation synthesis with cold sintering at room temperature. Once the HAp synthesis conditions were optimized, dissolution-precipitation synthesis was implemented to produce a homogeneous hydroxyapatite/chitosan composite material able to mimic bone tissue composition. The synthesised powders were cold sintered at room temperature; the obtained materials were structurally characterized and used for mechanical tests to evaluate their behaviour in light of bone tissue engineering purposes.

2. Materials and methods

2.1. Raw materials and chemicals

Mussel shells were collected from a restaurant in Trento (Italy), cleaned under tap water and manually grinded with a scouring pad to remove the external black coating (*periostracum*). After being dried at 90 °C overnight, shells were crushed in a ball mill for 5 min using porcelain balls (diameter = 20 mm) to obtain a fine powder (<350 μm). Hydrochloric acid (HCl fuming 37%, for analysis, CAS 7647-01-0), sodium hydroxide (NaOH pellets for analysis, CAS 1310-73-2), phosphoric acid (H_3PO_4 75%, CAS 7664-38-2) and chitosan from shrimp shells (low-viscous, CAS 9012-76-4) were purchased from Merck KGaA (Darmstadt - DE).

2.2. Dissolution-precipitation synthesis of hydroxyapatite

Hydroxyapatite (HAp) powder was produced by dissolution-precipitation synthesis. 10 g of mussel shells were initially mixed with 600 ml of distilled water using a Biosan MM-1000 overhead stirrer at 350 rpm. The temperature of the suspension was kept constant at 25 °C with a Biosan MSH-300i hot plate while the pH was continuously monitored with a WTW inoLab pH 7110 digital pH-meter. Once the pH stabilized at about 9.7–9.8, 12.6 ml of 4.76 M H_3PO_4 solution were added to the suspension in order to have a Ca/P molar ratio of 1.67. Once the pH stabilized at around 4.1, 64.5 ml of 3 M HCl solution were also added to the synthesis media to completely dissolve the mussel shell powder, obtaining a crystal-clear solution (pH ~ 1.5). The precipitation of calcium phosphate was induced by the rapid addition of 96 ml of 2 M NaOH solution which increased the pH to 11.3. The obtained calcium phosphate suspension was then heated up to 45 °C under constant stirring at 600 rpm. About 100 ml of the suspension were collected after 5 min, 30 min, 1 h, 1.5 h, 2 h, 3 h, 4 h, 5 h and 6 h to investigate the crystallization and phase evolution of the precipitate. The collected suspension was centrifugated, washed and resuspended repeatedly with distilled water to completely remove NaCl residues. Finally, the ceramic slurry was placed in liquid nitrogen for 10 min and freeze-dried for 72 h. The 6 h dissolution-precipitation synthesis was repeated at least 4 times to investigate the crystallization and phase evolution and to prove the reproducibility of the synthesis.

2.3. Dissolution-precipitation synthesis of hydroxyapatite/chitosan composite

Similarly, the hydroxyapatite/chitosan composite powder was synthesised according to dissolution-precipitation following the aforementioned procedure. Chitosan powder was added (2, 5 and 10 wt% with respect to HAp) to the synthesis medium right after the addition of HCl solution. The synthesis medium was continuously stirred to complete dissolve chitosan, and then NaOH solution was added to induce the calcium phosphate/chitosan precipitation. The composite suspension was stirred at 600 rpm for 1 h at 45 °C, before undergoing centrifugation, washing, liquid N_2 freezing and freeze-drying for 72 h. The synthesised composites were labelled as HAp2Chit, HAp5Chit and HAp10Chit according to the chitosan content.

2.4. Characterization of the as-synthesised powders

The as-synthesised powders were analysed by X-ray diffraction (XRD) by using a PANalytical Aeris diffractometer (Malvern Panalytical Ltd) equipped with a Cu source (Kα = 8.04 keV) and operating at 40 kV and 30 mA. XRD collected data were then processed by HighScore software (Malvern Panalytical Ltd). The reference patterns were obtained from the International Centre for Diffraction Data (ICDD®) database. The Ca/P molar ratio was determined with inductively coupled plasma - optical emission spectroscopy (ICP-OES) using a Spectro Ciros Vision CDD equipment by Spectro Analytical Instruments GmbH & Co. Three different HAp powder batches were analysed. For the analysis, about 300 μg of material were poured into a 100 ml flask and dissolved by the addition of 10 ml of nitric acid solution (5%) and ultra-pure water (conductivity <0.1 μS). From the 100 ml flask, 1 ml of solution was collected and poured into a 25 ml flask where additional 0.25 ml of nitric acid was added. Then, ultra-pure water was added to complete volume. The prepared solution was finally used for the analysis. Pure hydroxyapatite (>99.995% trace metal basis, CAS 12167-74-7, Sigma–Aldrich) was used as a standard to determine the Ca and P content in the material, while other possible elements were identified with a multi-element standard solution (type IV, Merck KGaA).

The functional groups of the as-synthesised powders were identified by Fourier-transformed infrared spectroscopy (FTIR) in the 4000 - 400 cm^{-1} range with a resolution of 4 cm^{-1} (64 scans) using a Thermo Scientific Nicolet iS50 FT-IR spectrometer. To perform the FTIR analysis in transmittance mode, few micrograms of the produced powder were mixed with about 0.3 g potassium bromide (KBr) and compacted under

50 kN to produce a pellet suitable for the test. The thermal evolution of the material was investigated by differential scanning calorimetry and thermogravimetric analysis (DSC-TGA) using a METTLER TOLEDO TGA/DSC 3+, STAR^e System thermobalance. About 10 mg of powder was poured into an alumina crucible and heated up to 1200 °C at 10 °C/min under an air flow of 10 ml/min. The morphology of the produced powder was assessed by field-emission scanning electron microscopy (FESEM) using a MIRA\LMU TESCAN microscope. The powders were coated with a thin layer of gold in an EMITECH K550X sputter coater to make the samples electrically conductive. Moreover, the specific surface area (SSA) of the powder was determined via the Brunauer–Emmett–Teller (BET) model by using Quadrasorb SI surface area and pore size analyser operating with nitrogen at −196 °C. According to ISO 9277:2010 standard, about 0.2 g of powders were degassed for 24 h at 25 °C with an Autosorb Degasser by Quantachrome Instruments before proceeding with the nitrogen absorption measurements. Based on the measured SSA value, the average particle size (D) was calculated under the hypothesis of spherical particle as

$$D = \frac{6}{SSA\,\rho} \quad \text{Eq.(1)}$$

where ρ is the real density of the powder. This latter was measured by Helium pycnometry with a Micro UltraPyc™ 1200e pycnometer (Quantachrome Instruments) for both synthesised HAp and HAp/chitosan composite. The measurement was considered valid only when five subsequent runs had a standard deviation smaller than 0.1%. The measurement was repeated at least three times per sample batch. In addition, the theoretical density of the HAp composites (ρ_{Comp}) was calculated according to the rule of mixtures as

$$\rho_{Comp} = \rho_{HAp}\nu_{HAp} + \rho_{Pol}\nu_{Pol} \quad \text{Eq.(2)}$$

where ρ_{HAp} is the real density of HAp, ρ_{Pol} the real density of the polymer, ν_{HAp} the volumetric fraction of HAp and ν_{Pol} the volumetric fraction of the polymeric filler.

2.5. Cold sintering of HAp and HAp composites

About 0.4 g of as-synthesised HAp powder was poured into a cylindrical die (diameter = 13 mm) and pressed up to 1500 MPa with a PW 100 ES two-column electrohydraulic lab press provided by P/O WEBER. The process was carried out at room temperature with 10 min holding time. The same procedure was carried out to consolidate the HAp/Chitosan composites.

2.6. Characterization of cold-sintered HAp and HAp composites

Cold sintered samples were analysed by XRD and FTIR to investigate possible phase transformations during sintering. The pellets density was determined according to ASTM C373-18 standard, using distilled water as an immersion medium. The samples were dried at 40 °C overnight prior to be measured. The material consolidation after cold sintering was assessed by FESEM, analysing the cross-section of sintered pellets.

Biaxial flexural strength was measured by the piston-on-three-balls method [60,61] using a Tinius Olsen MODEL 25ST mechanical testing machine. The crosshead speed was set at 0.33 mm/min. The pellets were first dried overnight at 40 °C and then coated with a thin polymeric tape to guarantee a uniform load distribution of the piston tip. The flexural strength (σ_f) was calculated from the failure load (P) as

$$\sigma_f = -0.2387\left[\frac{P(X-Y)}{d^2}\right] \quad \text{Eq.(3)}$$

where

$$X = (1+\nu)\ln(b/R)^2 + [(1-\nu)/2](b/R)^2 \quad \text{Eq.(3a)}$$

$$Y = (1+\nu)\left[1+\ln(a/R)^2\right] + (1-\nu)(a/R)^2 \quad \text{Eq.(3b)}$$

d being the thickness of the sample at fracture origin , a the radius of the support circle, b the radius of the ram tip, R the radius of the specimen and ν the Poisson's ratio (0.27 for hydroxyapatite [62]). At least nine replicates were tested for each sample. Starting from the collected mechanical data, the failure probability was calculated as

$$P_f = \frac{j-0.5}{N} \quad \text{Eq.(4)}$$

where j is the rank in the ascending ordered strength distribution and N is the total number of tested samples. The failure probability (P_f) can be correlated to the tensile stress (σ) through the Weibull distribution as

$$P_f = 1 - exp\left[-\left(\frac{\sigma}{\sigma_\theta}\right)^m\right], \sigma > 0 \quad \text{Eq.(5a)}$$

$$P_f = 0, \sigma \le 0 \quad \text{Eq.(5b)}$$

where σ_θ is the scale parameter (or Weibull characteristic strength) and m is the shape parameter (or Weibull modulus). Both Weibull modulus and characteristic strength were calculated by fitting the distribution after linearizing Eq. (5a) as

$$\ln\left(-\ln\left(1-P_f\right)\right) = m(\ln\sigma/\sigma_\theta) \quad \text{Eq.(6)}$$

after substituting the tensile stress with the flexural strength.

The fracture surface of mechanically tested samples was analysed by FESEM, after being coated with a thin gold layer. Sintered pellets were also subjected to a microhardness test, performed with a Mitutoyo Micro Vickers hardness testing machine (HM-200 Series). The applied load was 0.5 N. Before the test, the sample surface was polished using Buehler METADI® II diamond paste (6 and 1 μm) to a mirror finish. Vickers microhardness was determined from the applied load (F) and the diagonal length of the imprint (d), as

$$H_{Vickers} = 1.854\,\frac{F}{d^2} \quad \text{Eq.(7)}$$

The test was carried out on three replicates per HAp and HAp/Chitosan samples, and six imprints were performed on the surface of each sample.

Finally, the sintered composites were immerged in 13 ml of simulated body fluid (SBF) and were kept in an incubator at 37 °C under continuous shaking for 7 days to determine the polymer swelling [63]. SBF was prepared according to Kokubo et al. [63]. The dry mass of the samples was measured before immersion (w_{dry}) while the saturated mass (w_{sat}) was determined at each time point (day 1, 3, 5 and 7 after immersion) after gently blotting the sample surface with a microfiber cloth to remove the visible fluid [64,65]. The swelling ratio was calculated as

$$Swelling\ ratio = \frac{(w_{sat} - w_{dry})}{w_{dry}} \quad \text{Eq.(8)}$$

At day 7, the samples were also subjected to piston-on-three-ball test to investigate the evolution of the mechanical strength. Furthermore, the surface of cold-sintered pellets was observed by FESEM to detect the formation of new apatite layer after 24 h in SBF.

The mechanical data were reported as mean value ± standard deviation and statistically treated by ordinary one-way ANOVA and Dunnett's multiple comparison tests. Results were considered as significantly different for a p-value <0.05. The data analysis was performed with GraphPad Prism 9 software by Dotmatics.

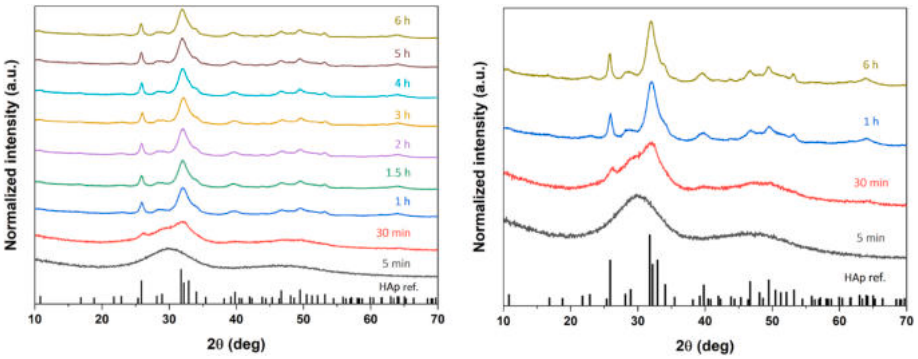

Fig. 1. a) XRD patterns of dissolution-precipitation synthesis (stirring time from 5 min to 6h), b) XRD patterns illustrating the vital time points in ACP to apatite transformation (the HAp reference pattern n° 00-064-0738 from ICDD® database is also reported).

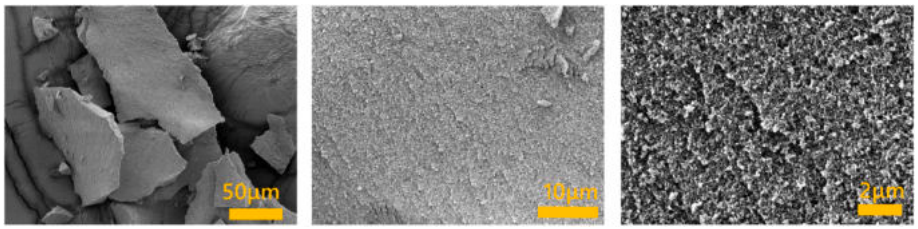

Fig. 2. FESEM images of as-synthesised HAp powder with precipitation stirring time of 1 h.

3. Results & discussions

3.1. Dissolution-precipitation synthesis of hydroxyapatite

The as-synthesised powder was analysed by X-ray diffraction to identify the crystalline phases. As shown in Fig. 1, amorphous calcium phosphate (ACP) is the first phase forming after the precipitation as demonstrated by two broad humps typical of ACP [66,67]. ACP is found to gradually transform into hydroxyapatite within 1 h at 45 °C, as confirmed by the comparison with the HAp reference pattern (HAp – ref. 00-064-0738). According to the XRD patterns obtained from several synthesis repetitions (Fig. S1), the turning point of ACP-to-HAp transformation seems to be around 30 min. HAp does not undergo any other phase transformation even after 6 h stirring at 45 °C, but its crystallinity increases as revealed by the more defined XRD peaks (Fig. 1b). The ACP-to-HAp transformation and the increase in HAp crystallinity for longer stirring time (or ripening) was also observed by Córdova-Udaeta et al. [68], who performed HAp precipitation at pH ranging around 10–11 at 60 °C. Based on these results, the dissolution-precipitation synthesis of hydroxyapatite proposed in this work is demonstrated to be reproducible and robust. For all subsequent syntheses, the precipitation time was set at 1 h because it was the minimum precipitation time to synthesise HAp in all repetitions (Fig. S1).

As mentioned, the HAp peaks in the XRD patterns (Fig. 1b) appear more defined and sharper by increasing the stirring time up to 6 h. Conversely, the XRD diffractogram of HAp produced with 1 h stirring time is characterized by quite broad XRD peaks, which can be due to a residual fraction of ACP. Such hypothesis is consistent with previous studies by Ressler et al. [69] and Brahimi [70], where, in addition to HAp, 10–20 wt% ACP was found after wet precipitation synthesis. Diffraction peak broadening is also typical for nanometric powders. The average powder particle size as calculated from the SSA measurement is $(242 \pm 1)\ m^2/g$, which corresponds to a spherical particle size of ~9 nm. In agreement, a fine hydroxyapatite powder with a nanometric particle size of ~13 nm [69] and ~18 nm [71] was also previously obtained by wet precipitation synthesis. The nanometric size is most likely the reason why powder particles appear highly agglomerated in the FESEM micrographs shown in Fig. 2.

The produced powder was further investigated by FTIR spectroscopy, as shown in Fig. 3. FTIR spectra further confirm the formation of the ACP at the beginning of precipitation and its crystallization into HAp already after 1 h (Fig. 3a). Both ACP and HAp spectra in Fig. 3b are

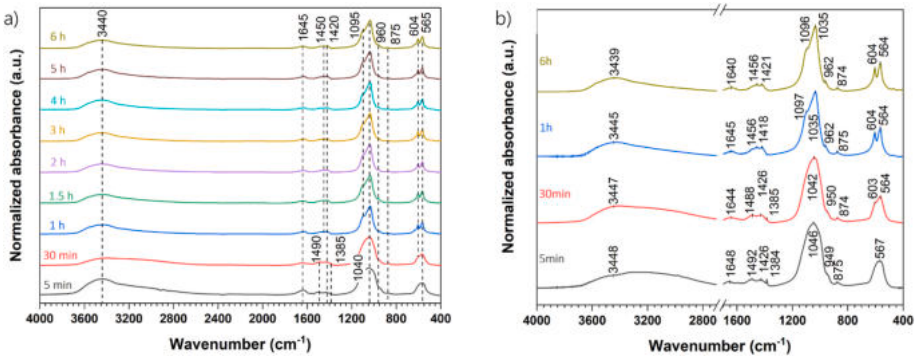

Fig. 3. a) FTIR spectra of powder obtained by dissolution-precipitation synthesis with a precipitation stirring time from 5 min to 6h; b) FTIR spectra of powder obtained after 5 min (ACP), 30 min, 1 h and 6 h of precipitation.

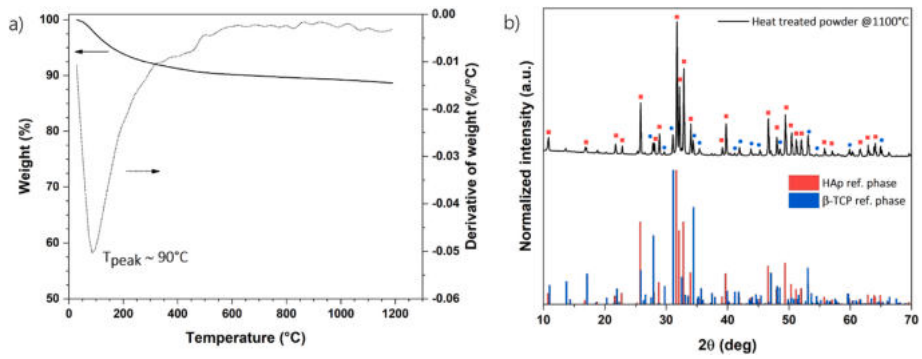

Fig. 4. a) Thermogravimetric curve (solid line) and corresponding derivative (dots line) of HAp (1 h precipitation), b) XRD pattern of HAp after thermal treatment at 1100 °C (HAp and β-TCP reference patterns n° 00-064-0738 and n° 01-072-7587 from ICDD® database are also shown).

characterized by bending peaks of absorbed and structural water (~3440 cm^{-1} and ~1645 cm^{-1}) and by phosphate signals of ν3-stretching **(1096 cm^{-1} and 1035 cm^{-1} for HAp, 1046 cm^{-1} for ACP** [66,67]**), ν1-stretching (962 cm-1 for HAp and 949 cm-1 for ACP** [66,67]**)** and ν4-bending (603 cm^{-1} and 564 cm^{-1} for HAp, and only 567 cm^{-1} for ACP [66,67]). The ACP and HAp spectra reported in this work agree with those found in the literature [66]. Moreover, bending bands associated with carbonate groups were also identified at 1453 cm^{-1}, 1420 cm^{-1}, and 875 cm^{-1}. Such bands are typically observed in B-type carbonate substituted HAp where $(CO_3)^{2-}$ groups replace phosphate ions [72,73]. The presence of carbonates is due to the use of mussel shells-derived calcium carbonate as raw material for the dissolution/precipitation synthesis. In agreement with B-type carbonate hydroxyapatite, the Ca/P molar ratio is equal to 1.69 ± 0.01. The ICP-OES analysis also detected 0.42 ± 0.06 wt% of Na, 0.082 ± 0.003 wt% of Mg and 0.061 ± 0.002 wt% of Sr. Therefore, the synthesised HAp is a non-stoichiometric, carbonated and multi-ion substituted hydroxyapatite with low crystallinity tenor, which resembles the characteristic features of bone apatite; it is expected to be more soluble, and consequently, more bioresorbable and osteoconductive than stoichiometric HAp [72–75].

The thermal evolution of the as-synthesised HAp was assessed by TGA analysis, shown in Fig. 4a. Pure HAp is characterized by a total weight loss of 11% from room temperature to 1200 °C. Most of the loss (~8% up to 300 °C) is due to the evolution of adsorbed and structural water [76] which has a maximum rate at ~90 °C according to the derivative of the TGA curve (dots line in Fig. 4a). The residual loss (~3%) could be associated with the carbonate degradation and to the dehydroxylation due HAp-to-β-TCP phase transformation [72,73,77]. Fig. 4b shows the XRD pattern of HAp powder after a thermal treatment at 1100 °C for 1 h (at 5 °C/min), where β-TCP (~9 wt%) phase was detected in addition to HAp. Moreover, diffraction peaks become sharper in shape (in comparison to Fig. 1b), consistently with a fully crystallization of HAp and with particle size coarsening at high temperature.

Table 1
Weight loss and enthalpy associated with chitosan degradation in HAp/Chitosan powder.

Sample	Weight loss in the range 250–400 °C (%)	ΔH (J/g)
HAp2Chit	~3	~27
HAp5Chit	~6	~116
HAp10Chit	~9	~252

Finally, the true density of the synthesised HAp determined by He pycnometry is equal to (2.68 ± 0.02) g/cm^3, which differs from the theoretical density of hydroxyapatite reported in the literature (3.16 g/cm^3) [62,78]. Analogously, Ortali et al. [79] and Lafon et al. [80] reported a true density of carbonated HAp powders produced by precipitation method at 90 °C equal to 2.94 g/cm^3 and 2.83 g/cm^3, respectively. The reason of the mismatch with respect to the HAp theoretical density could be related to the low-crystalline nature of the as-synthesised powder, as well as to its ion-substitution degree [80] and water content in the structure [81]; a certain degree of residual closed porosity in the agglomerated powder can also be considered.

3.2. Dissolution-precipitation synthesis of HAp/chitosan composite

As said, also HAp/chitosan composite powder was produced by dissolution-precipitation synthesis. The slurry was collected after 1 h from the beginning of precipitation at 45 °C. Fig. 5a shows the XRD diagrams of HAp/chitosan composites and of pure HAp and chitosan. All XRD peaks in the pattern are associated with the HAp reference phase. The relative amount of chitosan in the composite powder was investigated by DSC and TGA, as shown in Fig. 5b. In comparison with pure HAp, the HAp/chitosan composite powders show an additional mass

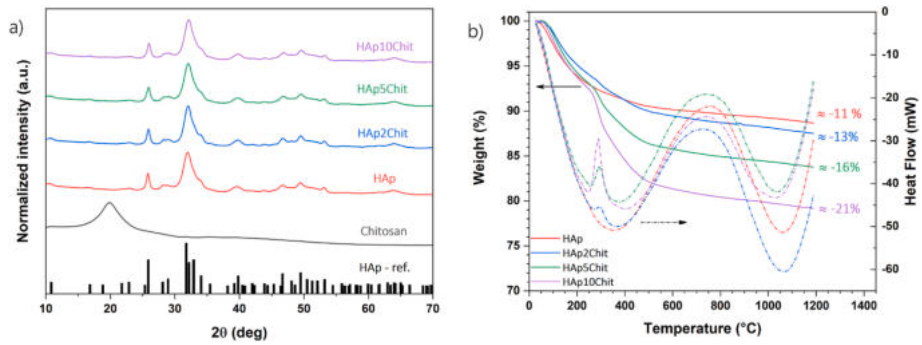

Fig. 5. a) XRD patterns of HAp/Chitosan composite powders (HAp reference pattern n° 00-064-0738 from ICDD® database is also reported); b) TGA-DSC curves of HAp/Chitosan composite powders; the weight loss values at 1200 °C are shown.

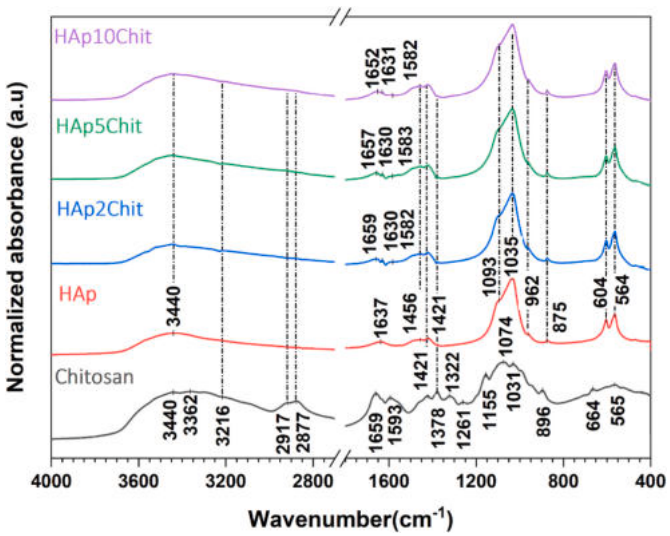

Fig. 6. FTIR spectra of chitosan, HAp and HAp/chitosan powders.

Table 2
Theoretical and real density of HAp, SSA and particle size of HAp and HAp/Chitosan powders.

Sample	Theoretical real density (g/cm^3)	Real density (g/cm^3)	SSA (m^2/g)	Estimated particle size (nm)
HAp2Chit	2.63	2.63 ± 0.01	165 ± 1	14
HAp5Chit	2.57	2.51 ± 0.01	155 ± 1	15
HAp10Chit	2.47	2.43 ± 0.01	151 ± 2	16

loss due to the polymer degradation between 250 °C and 400 °C corresponding to an exothermic peak in the DSC curves. Table 1 shows the enthalpy of the exothermic peak normalized with respect to the sample weight and the weight loss of the composites in the 250 °C–400 °C interval. Such weight loss is in good agreement with the amount of chitosan introduced during the synthesis.

The presence of the biopolymer was further confirmed by FTIR spectroscopy, as shown in Fig. 6. Chitosan is characterized by a broad band at 3400-3200 cm^{-1} due to stretching of OH groups and N–H vibrations, asymmetric and symmetric C–H stretching at respectively 2917 cm^{-1} and 2877 cm^{-1}, N–H bending signal at 1593 cm^{-1}, CH_3 bending at 1378 cm^{-1} and C–N stretching at 1031 cm^{-1} and bending at 896 cm^{-1} [82,83]. In addition, the absorbance band at 1659 cm^{-1} corresponds to C═O signal of amine type I, 1155 cm^{-1} and 1077 cm^{-1} peaks are ascribed to an antisymmetric stretch of C–O–C and C–N [84], while CH_2 bending and wagging is associated with the peak at 1421 cm^{-1} and at 1322 cm^{-1}, respectively [83,84]. In all composite powders, chitosan could be identified by characteristic peaks of N–H stretching at 3300-3200 cm^{-1}, asymmetric and symmetric C–H stretching at ~2920 cm^{-1} and ~2880 cm^{-1}, CH_3 bending at 1378 cm^{-1} and C═O band of amide-type I. Other infrared vibrations associated with chitosan were difficult to identify due to the overlapping with HAp signals. Interactions between hydroxyapatite and chitosan reported in the literature are of polar and/or ionic nature, involving Ca^{2+}, PO_4^{3-}, $–NH_2$, and –C═O groups [85,86]. Hydrogen bonds are also found between chitosan $–NH_2$ and hydroxyapatite –OH groups [86,87] and they are most likely responsible for the blue shift of C═O band of amine I group in the composites (~1650 cm^{-1}) with respect to the pure chitosan (~1660 cm^{-1}), in agreement with Ansari et al. [87] and Ressler et al. [88]. Conversely, the symmetric N–H bending signal of chitosan appears red-shifted from 1593 cm^{-1} to 1582 cm^{-1}. Also, the water bending vibration signal of HAp at 1637 cm^{-1} is red-shifted to ~1630 cm^{-1} in the composites. All these shifts of FTIR peaks suggest a possible interaction between HAp and chitosan in the composite materials.

Considering the real density of chitosan equal to (1.44 ± 0.01) g/cm^3, the theoretical real density of the composites was calculated by the rule of mixtures and then compared with that measured by He pycnometry. As reported in Table 2, there is a good agreement between theoretical and measured density. Similarly to pure HAp, composite nanopowders appear agglomerated as shown by FESEM micrographs in Fig. 7. The particle size of HAp/chitosan composite was determined by

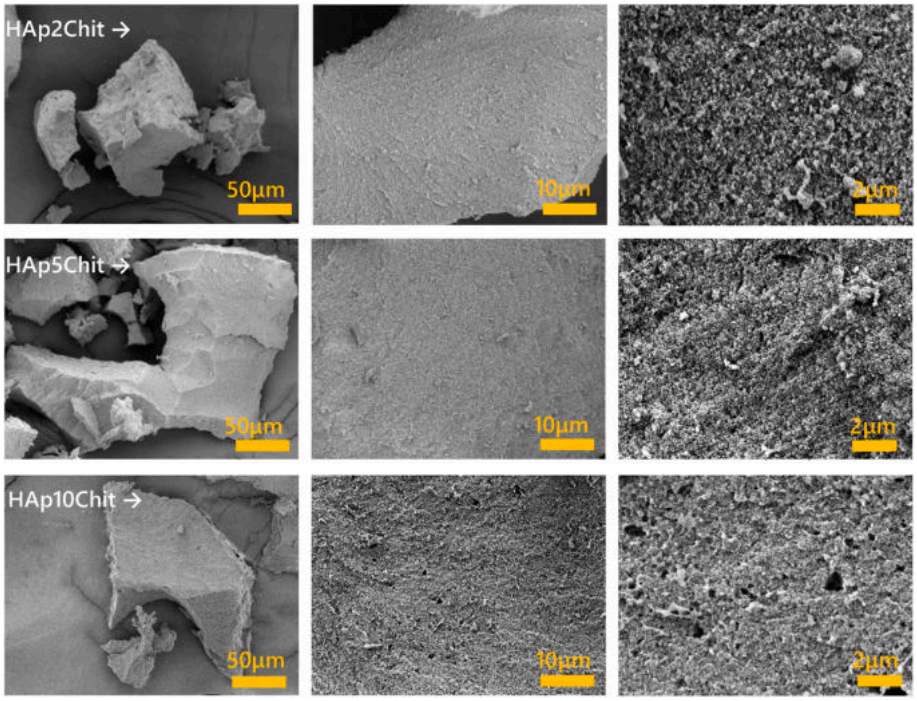

Fig. 7. FESEM images of HAp2Chit, HAp5Chit and HAp10Chit powder.

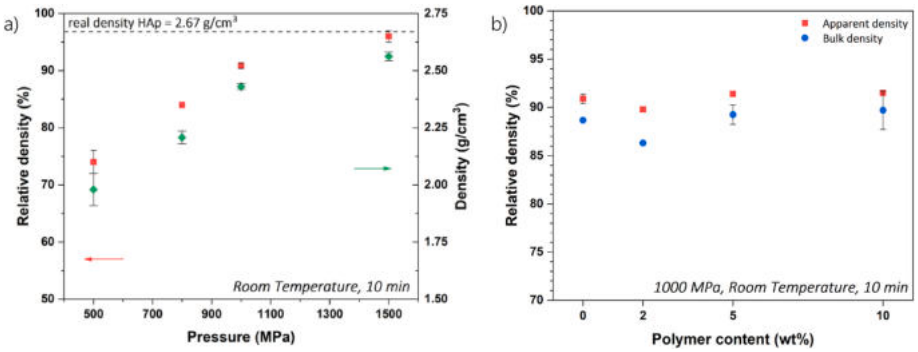

Fig. 8. a) Density of cold sintered HAp as a function of applied pressure, b) Relative density of HAp/Chitosan pellets sintered at room temperature under 1000 MPa.

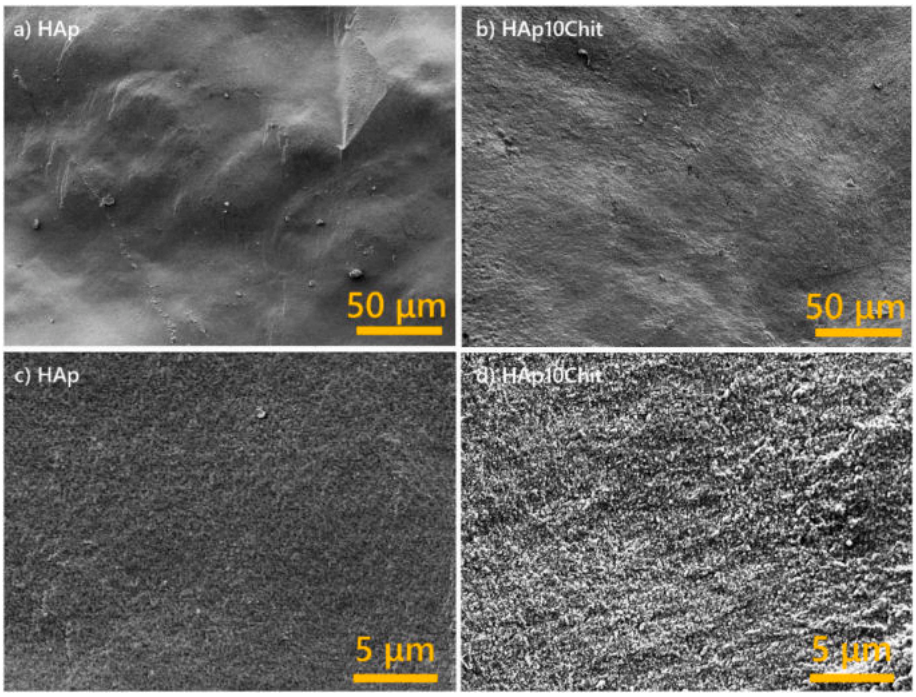

Fig. 9. Scanning electron microscopy of HAp (a and c) and HAp10Chit (b and d) pellet cross-section.

SSA measurements and their real density, resulting in a larger particle size with respect to HAp (Table 2). As previously reported by Rogina et al. [85], the larger particle size could be associated with the presence of chitosan, which offers a preferred site for nucleation and growth of HAp nanocrystals. In particular, the protonated amino groups of chitosan promote the formation of HAp due to their interaction with phosphate ions [85,86].

3.3. Characterization of cold sintered HAp and HAp/chitosan composite

HAp and HAp/chitosan powders were consolidated at room temperature by cold sintering. The material was actually pressed without the addition of any external solvent (like in the typical cold sintering process by definition [49]) to carry out the process at room temperature without any additional thermal treatment. A preliminary cold sintering test was carried out with variable increasing pressure to investigate its effect on the consolidation of HAp. The bulk density of the consolidated pellets is reported in Fig. 8a. The relative density was calculated according to the real density of the powders (Table 2). As shown in Fig. 8a, there is a densification of the material (from (74 ± 3)% to (96 ± 1)% relative density) by increasing the pressure from 500 MPa to 1500 MPa. However, the applied pressure for the successive experiments was set to 1000 MPa, because above this threshold the pellets were proner to develop surface defects, very likely because of intense spring-back effects. It is important to point out that the HAp consolidation achieved at room temperature in the present work is comparable to the cold sintering of HAp powder obtained previously at 500 MPa and 200 °C [55,56] and at 600 MPa at 150 °C [54]. Furthermore, the material consolidation (in terms of relative density) achieved by cold sintering at room temperature is higher in comparison to HAp sintered at 1100 °C for 2 h by solid state sintering (~88%) [89] and at 150 °C by spark plasma sintering (~50%) [79], whereas it is comparable with heat-treated HAp at 1200 °C by conventional sintering (~94%) for 2 h [89,90], and by flash sintering at 1160 °C (~91%) and at 1255 °C (~88%) for 10 s with a current density of 3 mA/mm^2 and 24 mA/mm^2, respectively [90].

Under 1000 MPa pressure, composite samples were sintered up to a relative density between 89% and 92%, as shown in Fig. 8b. In agreement, the cross-section of HAp and HAp10Chit pellet is reported in Fig. 9, where the micrographs show a quite high and uniform densification of the material, with no pores (Fig. 9a and b). Despite the intense pressure applied, no grains orientation can be clearly observed, even at higher magnification (Fig. 9c and d).

The consolidation during cold sintering is due to a synergistic effect of pressure, temperature and added liquid phase, being pressure-

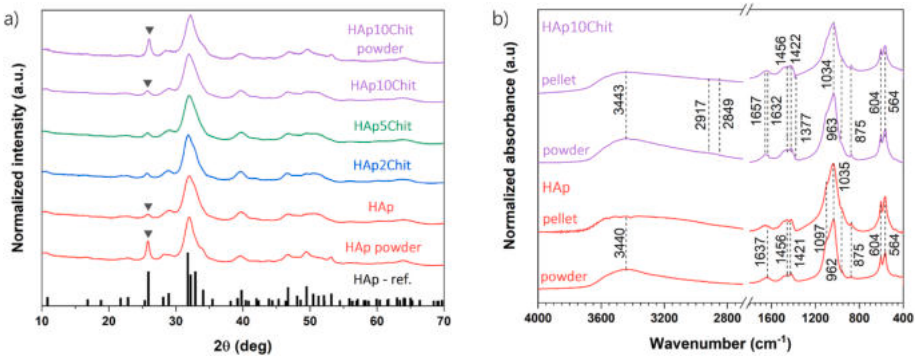

Fig. 10. a) XRD of sintered pellets at room temperature under 1000 MPa (HAp reference pattern n° 00-064-0738 in ICDD® database), b) FTIR spectra of sintered pellets under 1000 MPa in comparison to as-synthesised powder.

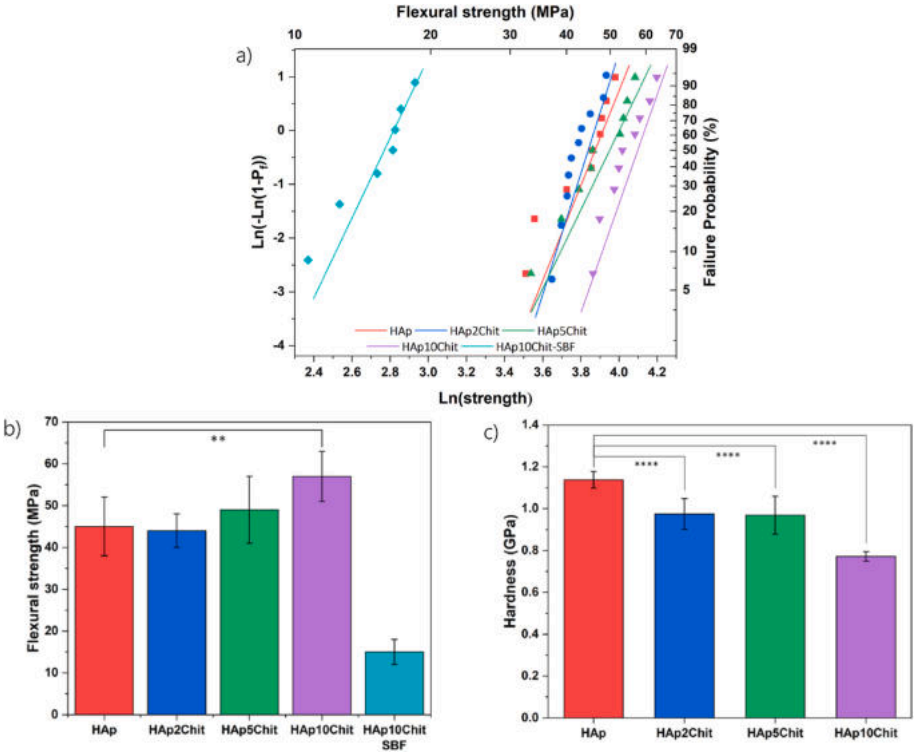

Fig. 11. a) Weibull distribution plot showing the failure probability as function of flexural strength of HAp/Chit sintered pellets (HAp10Chit pellets were tested in dry condition and after 7 days immersion in SBF solution), b) Flexural strength of HAp/Chit sintered pellets (HAp10Chit pellets were tested in dry condition and after 7 days immersion in SBF solution), c) Microhardness of HAp/chitosan composites (**: p-value<0.005, ****: p-value<0.0001).

solution creep and plastic deformation the concurrent densification mechanisms [53,91–93]. However, plastic deformation plays the major role in densification due to the absence of added liquid phase and of applied temperature in the present work. The densification is triggered by the intense applied pressure in addition to the fine nanometric particle size of the as-synthesised HAp and composites. The pellet density was measured by the Archimedes' method, revealing about 3–5% open pores in the composite material. Interestingly, the consolidated composites show a porosity and a density very close to those of natural cortical bone [94].

Sintered pellets did not undergo any phase transformation during sintering, as demonstrated by the XRD patterns in Fig. 10a. Nevertheless, the intensity of the peaks, especially that at 26°, decreases in the sintered bodies, possibly due to material's orientation, grain refinement and induced strain caused by the intense deformation as previously reported by Liu et al. [95]. The stability of HAp and composite after cold sintering was further confirmed by the FTIR spectra reported in Fig. 10b. The material stability after sintering is a remarkable feature of cold sintering and it highlights its potential in the consolidation of metastable materials and temperature sensitive systems [51,52,96]. In the specific case of bone-like apatite, the control over the sintering process is crucial, not only because the material could easily undergo phase transformation and grain coarsening but also because osteoconductivity is compromised by heat treatments [44]. Phase transformation associated with volume variation could cause cracks in the component, and grain growth is well-known to negatively affect the mechanical performance of the material [97].

3.4. Mechanical characterization of the cold sintered HAp and HAp/chitosan composite materials

The sintered samples were subjected to the piston-on-three-ball mechanical test to determine the biaxial flexural strength. The mechanical data are reported by Weibull plots as shown in Fig. 11. The

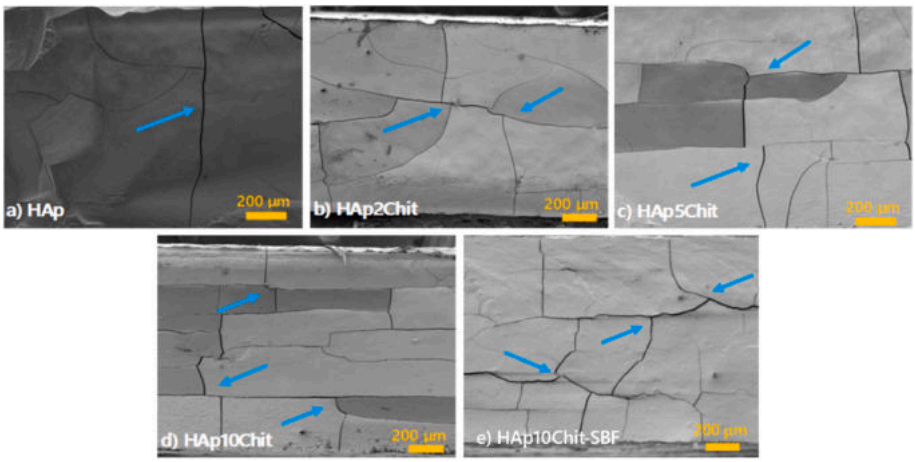

Fig. 12. FESEM of the cross section of HAp and HAp/Chitosan sintered pellets (a to d) and (e) HAp10Chit after SBF immersion and piston-on-three-ball test.

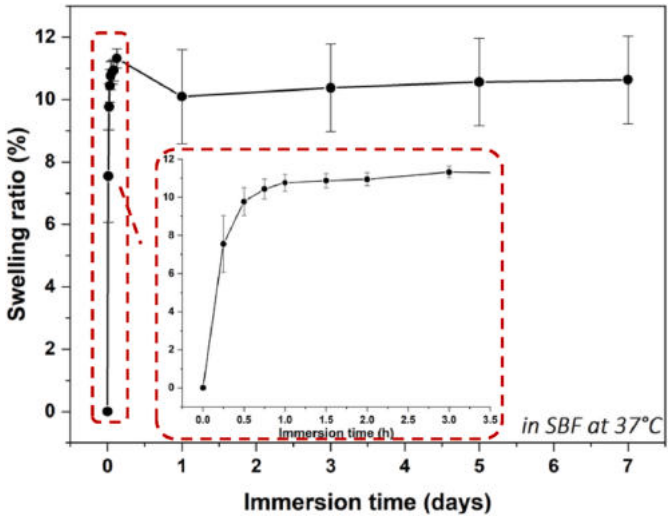

Fig. 13. Swelling ratio of HAp10Chit after immersion in SBF at 37 °C.

larger the polymer content, the higher the mechanical resistance of the material. Correspondingly, the average flexural strength is (45 ± 7) MPa for HAp, and (44 ± 4) MPa, (49 ± 8) MPa and (57 ± 6) MPa for HAp composite with 2, 5, and 10 wt% chitosan content, respectively. The Weibull modulus *m*, which estimates the scatter of the mechanical data and corresponds to the slope of the lines in Fig. 11a, is equal to ~9.1 for HAp, ~11.5 for HAp2Chit, ~7.5 for HAp5Chit, ~10.4 for HAp10Chit and ~7.6 for HAp10Chit-SBF. It is interesting to point out that the mechanical resistance of HAp sintered at room temperature in this work is larger than in HAp sintered at 900 °C in previous works (~30 MPa [98]), at 1000 °C (~40 MPa [98]), and at 1250 °C (~50 MPa [99]). Therefore, cold sintering allows not only to strongly reduce the processing time and temperature but also to produce quite dense HAp bodies, having even better mechaical performance than solid state sintered HAp. The larger mechanical resistance of the composites can be further justified by analysing the fracture surfaces of tested samples in Fig. 12. Cracks can be clearly observed in all the micrographs as indicated by the arrows, but more diffuse fragmentation is found in the composite samples by increasing the chitosan content. Such observation is consistent with the larger strength exerted by the material thanks to the presence of the polymer.

However, HAp2Chit and HAp5Chit show a mechanical resistance statistically comparable to HAp according to the ordinary one-way ANOVA test results (Fig. 11b). This means that HAp, HAp2Chit and HAp5Chit behaves practically in the same way under bending load application and therefore, the presence of 2 and 5 wt% chitosan does not compellingly improve the mechanical response of the ceramic material. Conversely, the flexural strength is significantly improved by adding 10 wt% chitosan. Hardness was also affected by the addition of the polymer, as shown in Fig. 11c. The microhardness of hydroxyapatite is equal to (1.14 ± 0.04) GPa, while it gradually decreases with the chitosan content to (0.97 ± 0.07) GPa for HAp2Chit, (0.97 ± 0.09) GPa for HAp5Chit and (0.77 ± 0.02) GPa for HAp10Chit. The measured hardness values are consistent with the hardness of natural apatite found in cortical bone of porcine, bovine and deer [100–103], and are close to the human bone hardness reported in the literature [104,105]. Zysset et al. [104] reported an average hardness value which ranges from ~0.2 GPa to ~ 0.8 GPa depending on the mineralization level, whereas Wu et al. [105] indicate a hardness of (0.33 ± 0.06) GPa for the proximal metaphysis, (0.42 ± 0.05) GPa for the diaphysis and (0.35 ± 0.05) GPa for the distal metaphysis.

With an eye to possible biomedical applications, HAp and HAp10Chit samples were also tested in vitro to investigate their behaviour under simulated physiological conditions. As shown in Fig. 13, the composite pellets swelled of ~10% after immersion in SBF at 37 °C, this occurring in about 3.5 h with no further variations during the following 7 days. HAp and HAp10Chit pellets developed a thin apatite layer on their surface after 24 h immersion in SBF as shown by the SEM micrographs in Fig. 14, similarly to previous activities [106–108].

The formation of the apatite layer was confirmed by XRD analyses (Fig. S2). Since the SBF immersion test is one of the most accepted and widespread assay to prove material bioactivity [109], the produced HAp and HAp/Chitosan composites can be truly addressed as bioactive. After 7 days soaking in SBF, HAp10Chit samples saturated with the fluid were subjected to flexural bending test. The measured strength is (15 ± 3) MPa after SBF immersion, much lower than the values determined in dry conditions (Fig. 11 a). Such decrease in mechanical resistance could be associated with (i) swelling, (ii) formation of the surface apatite layer, (iii) the presence of the fluid in open pores (accounting for capillary forces) and (iv) additional pore formation due ions diffusion from the pellet to the SBF solution [39,107,110]. A reduction of mechanical strength after SBF soaking has been previously observed and correlated to porosity and surface reaction after the immersion in SBF [110,111]. The SEM micrographs in Fig. 12e show the fracture surface of HAp10Chit after SBF immersion. Like for the composite pellet tested in dry conditions, the cross-section is characterized by microcracks, formed as consequence of the bending load applied but also as a result of SBF immersion as previously reported by Gu et al. [110]. The mechanical properties evaluation after soaking in SBF solution is rarely reported in the literature but it should be a fundamental criterion to properly

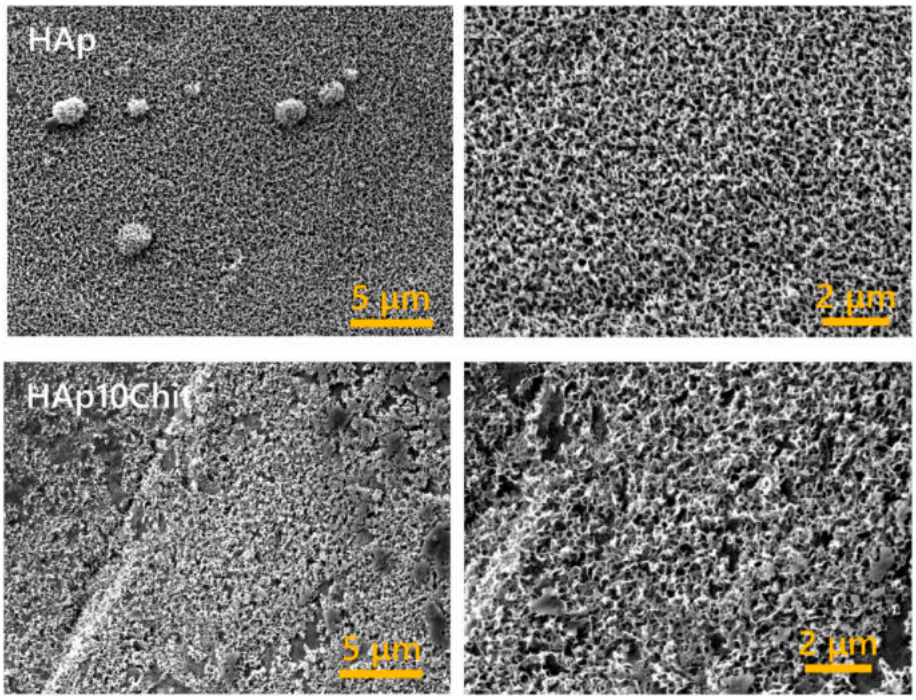

Fig. 14. Scanning electron microscopy of HAp and HAp10Chit pellet surface after SBF immersion at 37 °C for 24h.

address bone tissue applications. Nonetheless, future works should involve the cold sintered materials response in in-vitro cell studies, such as adhesion, proliferation and differentiation of mesenchymal stem cells possibly. However, the absence of macropores (100–900 μm) suitable for cell migration and bone ingrowth is a limitation for bone tissue engineering scaffolds [112,113] despite the high relative density achieved in the present work. Therefore, bioactive coatings for metallic (i.e. Ti-alloys) or inert (i.e. alumina, zirconia) implants could be foreseen as an appropriate future biomedical application for bioceramics densified by cold sintering. Alternatively, macropores formation in vitro could be also explored in the future by the introduction of a pore-forming additives able to dissolve and form pores without causing the disintegration of the scaffold.

4. Conclusions

In the present work, biogenic hydroxyapatite and hydroxyapatite/chitosan composites were successfully produced by dissolution-precipitation synthesis, where natural calcium carbonate was obtained by mussel shells and chitosan was derived from shrimp shells deacetylation. For the first time, hydroxyapatite and hydroxyapatite/chitosan composite were cold sintered at room temperature up to 90% relative density in only 10 min. HAp/Chitosan composite processed in the current study could be a valid future candidate for bone tissue regeneration, especially for cortical bone. In fact, flexural strength and hardness of the composite material are compatible with the mechanical properties of compact bone. In addition, the bioactivity of HAp/chitosan composite was demonstrated by SBF immersion for 24 h, revealing the formation of a widespread thin layer of apatite on the surface of the samples. Considering the results of the present work as a starting point, *in-vitro* characterization involving cells studies on the material should be carried out in the near future.

Declaration of competing interest

The authors declare that they have no known competing financial interests or personal relationships that could have appeared to influence the work reported in this paper.

Acknowledgements

This work was supported by the Italian Ministry of University and Research (MIUR) within the “REGENERA” and “E-Mat” projects of the Departments of Excellence 2018–2022 (DII-UNITN). The authors are grateful to the JECS Trust for funding the visit of A. Galotta to Baltic Biomaterials Centre of Excellence of Riga Technical University (Contract No. 2021277). The authors acknowledge the access to infrastructure and expertise of the BBCE- Baltic Biomaterial Centre of Excellence (European Union’s Horizon 2020 research and innovation programme under the grant agreement No. 857287) and the financial support of RISEus2 (European Union’s Horizon 2020 research and innovation programme under the grant agreement No. 952347). The graphical abstract was created on Biorender.com.

Appendix A. Supplementary data

Supplementary data to this article can be found online at https://doi.org/10.1016/j.oceram.2023.100418.

References

[1] W.R. Stahel, The circular economy, Nature 531 (2016) 435–438, https://doi.org/10.1038/531435a.
[2] L. Wenhai, et al., Successful blue economy examples with an emphasis on international perspectives, Front. Mar. Sci. 6 (261) (2019) 1–14, https://doi.org/10.3389/fmars.2019.00261.
[3] D. Summa, M. Lanzoni, G. Castaldelli, E.A. Fano, E. Tamburini, Trends and opportunities of bivalve shells’ waste valorization in a prospect of circular blue bioeconomy, Resources 11 (48) (2022) 1–16, https://doi.org/10.3390/resources11050048.
[4] K.H. Mo, U.J. Alengaram, M.Z. Jumaat, S.C. Lee, W.I. Goh, C.W. Yuen, Recycling of seashell waste in concrete: review, Construct. Build. Mater. 162 (Feb. 2018) 751–764, https://doi.org/10.1016/j.conbuildmat.2017.12.009.
[5] S.I. Ahmad, et al., Chitin and its derivatives: structural properties and biomedical applications, Int. J. Biol. Macromol. 164 (Dec. 2020) 526–539, https://doi.org/10.1016/j.ijbiomac.2020.07.098.
[6] P. Terzioğlu, H. Öğüt, A. Kalemtaş, Natural calcium phosphates from fish bones and their potential biomedical applications, Mater. Sci. Eng. C 91 (May) (Oct. 2018) 899–911, https://doi.org/10.1016/j.msec.2018.06.010.
[7] T. Rustad, I. Storrø, R. Slizyte, Possibilities for the utilisation of marine by-products, Int. J. Food Sci. Technol. 46 (10) (Oct. 2011) 2001–2014, https://doi.org/10.1111/j.1365-2621.2011.02736.x.

[8] A. Kaanane, M. Hind, Valorization technologies of marine by-products, in: Innovation in the Food Sector through the Valorization of Food and Agro-Food By-Products, 2020.

[9] J.P. Morris, T. Backeljau, G. Chapelle, Shells from aquaculture: a valuable biomaterial, not a nuisance waste product, Rev. Aquacult. 11 (1) (2019) 42–57, https://doi.org/10.1111/raq.12225.

[10] M. chen Wan, et al., Biomaterials from the sea: uture building blocks for biomedical applications, Bioact. Mater. 6 (12) (2021) 4255–4285, https://doi.org/10.1016/j.bioactmat.2021.04.028.

[11] FAO.org. https://www.fao.org/fishery/statistics-query/en/home, 2022.

[12] M. Jović, M. Mandić, M.Š. Ivanović, I. Smičiklas, Recent trends in application of shell waste from mariculture, Stud. Marxism 32 (1) (2019) 47–62, https://doi.org/10.5281/zenodo.3274471.

[13] Y. Hou, et al., Marine shells: potential opportunities for extraction of functional and health-promoting materials, Crit. Rev. Environ. Sci. Technol. 46 (11–12) (2016) 1047–1116, https://doi.org/10.1080/10643389.2016.1202669.

[14] Yan Ning, Xi Chen, Sustainability: don't waste seafood waste, Nature 524 (2015) 155–157, https://doi.org/10.1038/524155a.

[15] C. Martínez-García, B. González-Fonteboa, F. Martínez-Abella, D. Carro- López, Performance of mussel shell as aggregate in plain concrete, Construct. Build. Mater. 139 (2017) 570–583, https://doi.org/10.1016/j.conbuildmat.2016.09.091.

[16] U.G. Eziefula, J.C. Ezeh, B.I. Eziefula, Properties of seashell aggregate concrete: a review, Construct. Build. Mater. 192 (2018) 287–300, https://doi.org/10.1016/j.conbuildmat.2018.10.096.

[17] C. Bremner, T.A. Cochrane, P. McGuigan, R. Bello-Mendoza, Removal of dissolved heavy metals from stormwater by filtration with granular recycled glass and mussel shell with and without microalgae biofilm, Environ. Technol. Innov. 18 (2020), 100662, https://doi.org/10.1016/j.eti.2020.100662.

[18] S. Abraham, S. Joslyn, I. H. Mel Suffet, Treatment of odor by a seashell biofilter at a wastewater treatment plant, J. Air Waste Manag. Assoc. 65 (10) (2015) 1217–1228, https://doi.org/10.1080/10962247.2015.1075918.

[19] M. Egerić, et al., Separation of Cu(II) ions from synthetic solutions and wastewater by raw and calcined seashell waste, Desalination Water Treat. 132 (2018) 205–214, https://doi.org/10.5004/dwt.2018.23131.

[20] C. Komintarachat, S. Chuepeng, Catalytic enhancement of calcium oxide from green mussel shell by potassium chloride impregnation for waste cooking oil-based biodiesel production, Bioresour. Technol. Reports 12 (2020), 100589, https://doi.org/10.1016/j.biteb.2020.100589.

[21] H. Hadiyanto, A.H. Afianti, U.I. Navi'A, N.P. Adetya, W. Widayat, H. Sutanto, The development of heterogeneous catalyst C/CaO/NaOH from waste of green mussel shell (Perna varidis) for biodiesel synthesis, J. Environ. Chem. Eng. 5 (5) (2017) 4559–4563, https://doi.org/10.1016/j.jece.2017.08.049.

[22] M. Mititelu, et al., Mussel shells, a valuable calcium resource for the pharmaceutical industry, Mar. Drugs 20 (25) (2022) 1–16, https://doi.org/10.3390/md20010025.

[23] M. Sari, P. Hening, Chotimah, I.D. Ana, Y. Yusuf, Bioceramic hydroxyapatite-based scaffold with a porous structure using honeycomb as a natural polymeric Porogen for bone tissue engineering, Biomater. Res. 25 (2) (2021) 1–13, https://doi.org/10.1186/s40824-021-00203-z.

[24] A. Shavandi, A.E.D.A. Bekhit, A. Ali, Z. Sun, Synthesis of nano-hydroxyapatite (nHA) from waste mussel shells using a rapid microwave method, Mater. Chem. Phys. 149 (150) (2015) 607–616, https://doi.org/10.1016/j.matchemphys.2014.11.016.

[25] M. Irfan, P.S. Suprajaa, R. Praveen, B.M. Reddy, Microwave-assisted one-step synthesis of nanohydroxyapetite from fish bones and mussel shells, Mater. Lett. 282 (2021), 128685, https://doi.org/10.1016/j.matlet.2020.128685.

[26] S.-W. Lee, et al., Comparative Study of hydroxyapatite prepared from seashells and eggshells as a bone graft material, Tissue Eng. Regen. Med. 11 (2) (Apr. 2014) 113–120, https://doi.org/10.1007/s13770-014-0056-1.

[27] I.J. Macha, L.S. Ozyegin, J. Chou, R. Samur, F.N. Oktar, B. Ben-Nissan, An alternative synthesis method for di calcium phosphate (monetite) powders from mediterranean mussel (mytilus galloprovincialis) shells, J. Australas. Ceram. Soc. 49 (2) (2013) 122–128.

[28] S. Owuamanam, D. Cree, Progress of bio-calcium carbonate waste eggshell and seashell fillers in polymer composites: a review, J. Compos. Sci. 4 (2) (Jun. 2020) 70, https://doi.org/10.3390/jcs4020070.

[29] F. Yang, D. Yang, J. Tu, Q. Zheng, L. Cai, L. Wang, Strontium enhances osteogenic differentiation of mesenchymal stem cells and in vivo bone formation by activating Wnt/catenin signaling, Stem Cell. 29 (6) (2011) 981–991, https://doi.org/10.1002/stem.646.

[30] K. Lin, et al., Strontium substituted hydroxyapatite porous microspheres: surfactant-free hydrothermal synthesis, enhanced biological response and sustained drug release, Chem. Eng. J. 222 (2013) 49–59, https://doi.org/10.1016/j.cej.2013.02.037.

[31] K. Lin, et al., Biomimetic hydroxyapatite porous microspheres with co-substituted essential trace elements: surfactant-free hydrothermal synthesis, enhanced degradation and drug release, J. Mater. Chem. 21 (41) (2011) 16558–16565, https://doi.org/10.1039/c1jm12514a.

[32] J. Sang Cho, et al., Enhanced osteoconductivity of sodium-substituted hydroxyapatite by system instability, J. Biomed. Mater. Res., Part B 102 (5) (2014) 1046–1062, https://doi.org/10.1002/jbm.b.33087.

[33] E. Boanini, M. Gazzano, A. Bigi, Ionic substitutions in calcium phosphates synthesized at low temperature, Acta Biomater. 6 (6) (2010) 1882–1894, https://doi.org/10.1016/j.actbio.2009.12.041.

[34] S.K.L. Levengood, M. Zhang, Chitosan-based scaffolds for bone tissue engineering, J. Mater. Chem. B 2 (21) (2014) 3161, https://doi.org/10.1039/c4tb00027g.

[35] Y.J. Seol, et al., Chitosan sponges as tissue engineering scaffolds for bone formation, Biotechnol. Lett. 26 (13) (2004) 1037–1041, https://doi.org/10.1023/b:bile.0000032962.79531.fd.

[36] P.R. Klokkevold, L. Vandemark, E.B. Kenney, G.W. Bernard, Osteogenesis enhanced by chitosan (poly-N-acetyl glucosaminoglycan) in vitro, J. Periodontol. 67 (11) (1996) 1170–1175, https://doi.org/10.1902/jop.1996.67.11.1170.

[37] X. Yang, X. Chen, H. Wang, Acceleration of osteogenic differentiation of preosteoblastic cells by chitosan containing nanofibrous scaffolds, Biomacromolecules 10 (10) (2009) 2772–2778, https://doi.org/10.1021/bm900623j.

[38] S. Mathews, P.K. Gupta, R. Bhonde, S. Totey, Chitosan enhances mineralization during osteoblast differentiation of human bone marrow-derived mesenchymal stem cells, by upregulating the associated genes, Cell Prolif. 44 (6) (2011) 537–549, https://doi.org/10.1111/j.1365-2184.2011.00788.x.

[39] A. Zima, Hydroxyapatite-chitosan based bioactive hybrid biomaterials with improved mechanical strength, Spectrochim. Acta Part A Mol. Biomol. Spectrosc. 193 (2018) 175–184, https://doi.org/10.1016/j.saa.2017.12.008.

[40] Y.P. Guo, J.J. Guan, J. Yang, Y. Wang, C.Q. Zhang, Q.F. Ke, Hybrid nanostructured hydroxyapatite-chitosan composite scaffold: bioinspired fabrication, mechanical properties and biological properties, J. Mater. Chem. B 3 (23) (2015) 4679–4689, https://doi.org/10.1039/c5tb00175g.

[41] H. Yilmaz Atay, S. Jana, Antibacterial activity of chitosan-based systems, in: Functional Chitosan: Drug Delivery and Biomedical Applications, Springer, 2019.

[42] M. Hosseinnejad, S.M. Jafari, Evaluation of different factors affecting antimicrobial properties of chitosan, Int. J. Biol. Macromol. 85 (2016) 467–475, https://doi.org/10.1016/j.ijbiomac.2016.01.022.

[43] M. Si, et al., Preparation of zinc oxide/poly-ether-ether-ketone (PEEK) composites via the cold sintering process, Acta Mater. 215 (2021), 117036, https://doi.org/10.1016/j.actamat.2021.117036.

[44] K. Ishikawa, Bone substitute fabrication based on dissolution-precipitation reactions, Materials 3 (2) (2010) 1138–1155, https://doi.org/10.3390/ma3021138.

[45] J. Vecstaudza, J. Locs, Novel preparation route of stable amorphous calcium phosphate nanoparticles with high specific surface area, J. Alloys Compd. 700 (2017) 215–222, https://doi.org/10.1016/j.jallcom.2017.01.038.

[46] A. Kizalaite, et al., Dissolution-precipitation synthesis and characterization of zinc whitlockite with variable metal content, ACS Biomater. Sci. Eng. 7 (8) (2021) 3586–3593, https://doi.org/10.1021/acsbiomaterials.1c00335.

[47] C. Vakifahmetoglu, L. Karacasulu, Cold sintering of ceramics and glasses: a review, Curr. Opin. Solid State Mater. Sci. 24 (1) (Feb. 2020), 100807, https://doi.org/10.1016/j.cossms.2020.100807.

[48] C.A. Randall, J. Guo, A. Baker, M. Lanagan, H. Guo, Cold Sintering Ceramics and Composites, 2017.

[49] J. Guo, et al., Cold sintering: a paradigm shift for processing and integration of ceramics, Angew. Chem. Int. Ed. 55 (38) (Sep. 2016) 11457–11461, https://doi.org/10.1002/anie.201605443.

[50] J. Guo, S.S. Berbano, H. Guo, A.L. Baker, M.T. Lanagan, C.A. Randall, Cold Sintering Process of Composites : Bridging the Processing Temperature Gap of Ceramic and Polymer Materials, 2016, pp. 7115–7121, https://doi.org/10.1002/adfm.201602489.

[51] S.H. Bang, T. Herisson De Beauvoir, C.A. Randall, Densification of thermodynamically unstable tin monoxide using cold sintering process, J. Eur. Ceram. Soc. 39 (4) (2019) 1230–1236, https://doi.org/10.1016/j.jeurceramsoc.2018.11.026.

[52] C. Yang, et al., ZrW2O8 with negative thermal expansion fabricated at ultralow temperature: an energy-efficient strategy for metastable material fabrication, ACS Sustain. Chem. Eng. 7 (17) (2019) 14747–14755, https://doi.org/10.1021/acssuschemeng.9b02682.

[53] A. Galotta, V.M. Sglavo, The cold sintering process: a review on processing features, densification mechanisms and perspectives, J. Eur. Ceram. Soc. 41 (16) (2021) 1–17, https://doi.org/10.1016/j.jeurceramsoc.2021.09.024.

[54] N. Guo, H.Z. Shen, P. Shen, Cold sintering of chitosan/hydroxyapatite composites, Materialia 21 (December 2021) (2022), 101294, https://doi.org/10.1016/j.mtla.2021.101294.

[55] M. ul Hassan, M. Akmal, H.J. Ryu, Cold sintering of as-dried nanostructured calcium hydroxyapatite without using additives, J. Mater. Res. Technol. 11 (2021) 811–822, https://doi.org/10.1016/j.jmrt.2021.01.060.

[56] H.Z. Shen, N. Guo, Y. Liang, P. Shen, Synthesis and densification of hydroxyapatite by mechanochemically-activated reactive cold sintering, Scripta Mater. 194 (2021), 113717, https://doi.org/10.1016/j.scriptamat.2020.113717.

[57] A. Galotta, F. Agostinacchio, A. Motta, S. Dirè, V.M. Sglavo, Mechanochemical synthesis and cold sintering of mussel shell-derived hydroxyapatite nano-powders for bone tissue regeneration, J. Eur. Ceram. Soc. 43 (2) (2023) 639–647, https://doi.org/10.1016/j.jeurceramsoc.2022.09.024.

[58] S. Al-Maawi, et al., Erratum: 'Thermal treatment at 500°C significantly reduces the reaction to irregular tricalcium phosphate granules as foreign bodies: an in vivo study' (Acta Biomaterialia (2022) 142 (413), (S1742706122000083), (10.1016/j.actbio.2022.01.008)), Acta Biomater. 142 (2022) 414–429, https://doi.org/10.1016/j.actbio.2022.01.011.

[59] R.J. Egli, S. Gruenenfelder, N. Doebelin, W. Hofstetter, R. Luginbuehl, M. Bohner, Thermal treatments of calcium phosphate biomaterials to tune the physico-chemical properties and modify the in vitro osteoclast response, Adv. Eng. Mater. 13 (3) (2011) 102–107, https://doi.org/10.1002/adem.201080037.

[60] A. Börger, P. Supancic, R. Danzer, The ball on three balls test for strength testing of brittle discs: stress distribution in the disc, J. Eur. Ceram. Soc. 22 (2002) 1425–1436, https://doi.org/10.1016/S0955-2219(01)00458-7.

[61] J.E. Ritter, K. Jakus, A. Batakis, N. Bandyopadhyay, Appraisal of biaxial strength testing, J. Non-Cryst. Solids 38 (39) (1980) 419–424, https://doi.org/10.1016/0022-3093(80)90455-X.

[62] N. Eliaz, N. Metoki, Calcium phosphate bioceramics: a review of their history, structure, properties, coating technologies and biomedical applications, Materials 10 (2017) 1–104, https://doi.org/10.3390/ma10040334.

[63] T. Kokubo, H. Takadama, How useful is SBF in predicting in vivo bone bioactivity? Biomaterials 27 (15) (2006) 2907–2915, https://doi.org/10.1016/j.biomaterials.2006.01.017.

[64] C. Xianmiao, L. Yubao, Z. Yi, Z. Li, L. Jidong, W. Huanan, Properties and in vitro biological evaluation of nano-hydroxyapatite/chitosan membranes for bone guided regeneration, Mater. Sci. Eng. C 29 (1) (2009) 29–35, https://doi.org/10.1016/j.msec.2008.05.008.

[65] A. Satpathy, et al., Bioactive nano-hydroxyapatite doped electrospun PVA-chitosan composite nanofibers for bone tissue engineering applications, J. Indian Inst. Sci. 99 (3) (2019) 289–302, https://doi.org/10.1007/s41745-019-00118-8.

[66] C. Combes, C. Rey, Amorphous calcium phosphates: synthesis, properties and uses in biomaterials, Acta Biomater. 6 (9) (2010) 3362–3378, https://doi.org/10.1016/j.actbio.2010.02.017.

[67] K. Rubenis, S. Zemjane, J. Vecstaudza, J. Bitenieks, J. Locs, Densification of amorphous calcium phosphate using principles of the cold sintering process, J. Eur. Ceram. Soc. 41 (1) (2021) 912–919, https://doi.org/10.1016/j.jeurceramsoc.2020.08.074.

[68] M. Córdova-Udaeta, Y. Kim, K. Yasukawa, Y. Kato, T. Fujita, G. Dodbiba, Study on the synthesis of hydroxyapatite under highly alkaline conditions, Ind. Eng. Chem. Res. 60 (11) (Mar. 2021) 4385–4396, https://doi.org/10.1021/acs.iecr.0c05969.

[69] A. Ressler, et al., From bio-waste to bone substitute: synthesis of biomimetic hydroxyapatite and its use in chitosan-based composite scaffold preparation, Chem. Biochem. Eng. Q. 34 (2) (2020) 59–71, https://doi.org/10.15255/CABEQ.2020.1783.

[70] S. Brahimi, et al., Preparation and characterization of biocomposites based on chitosan and biomimetic hydroxyapatite derived from natural phosphate rocks, Mater. Chem. Phys. 276 (August 2021) 2022, https://doi.org/10.1016/j.matchemphys.2021.125421.

[71] M. Lakrat, H. Jodati, E.M. Mejdoubi, Z. Evis, Synthesis and characterization of pure and Mg, Cu, Ag, and Sr doped calcium-deficient hydroxyapatite from brushite as precursor using the dissolution-precipitation method, Powder Technol. 413 (October 2022) (2023), 118026, https://doi.org/10.1016/j.powtec.2022.118026.

[72] K. Benataya, M. Lakrat, L.L. Elansari, E. Mejdoubi, Synthesis of B-type carbonated hydroxyapatite by a new dissolution-precipitation method, Mater. Today Proc. 31 (2020) S83, https://doi.org/10.1016/j.matpr.2020.06.100. –S88.

[73] E. Landi, G. Celotti, G. Logroscino, A. Tampieri, Carbonated hydroxyapatite as bone substitute, J. Eur. Ceram. Soc. 23 (15) (2003) 2931–2937, https://doi.org/10.1016/S0955-2219(03)00304-2.

[74] A. Rupani, L.A. Hidalgo-Bastida, F. Rutten, A. Dent, I. Turner, S. Cartmell, Osteoblast activity on carbonated hydroxyapatite, J. Biomed. Mater. Res., Part A 100 A (4) (2012) 1089–1096, https://doi.org/10.1002/jbm.a.34037.

[75] M.-M. Germaini, et al., Osteoblast and osteoclast responses to A/B type carbonate-substituted hydroxyapatite ceramics for bone regeneration, Biomed. Mater. 12 (3) (2017), https://doi.org/10.1088/1748-605X/aa69c3.

[76] H. zhen Shen, N. Guo, L. Zhao, P. Shen, Role of ion substitution and lattice water in the densification of cold-sintered hydroxyapatite, Scripta Mater. 177 (2020) 141–145, https://doi.org/10.1016/j.scriptamat.2019.10.024.

[77] T.I. Ivanova, O.V. Frank-Kamenetskaya, A.B. Kol'tsov, V.L. Ugolkov, Crystal structure of calcium-deficient carbonated hydroxyapatite. Thermal decomposition, J. Solid State Chem. 160 (2) (2001) 340–349, https://doi.org/10.1006/jssc.2000.9238.

[78] K.A. Hing, S.M. Best, W. Bonfield, Characterization of porous hydroxyapatite, J. Mater. Sci. Mater. Med. 10 (3) (1999) 135–145, https://doi.org/10.1023/A:1008929305897.

[79] C. Ortali, I. Julien, M. Vandenhende, C. Drouet, E. Champion, Consolidation of bone-like apatite bioceramics by spark plasma sintering of amorphous carbonated calcium phosphate at very low temperature, J. Eur. Ceram. Soc. 38 (4) (2018) 2098–2109, https://doi.org/10.1016/j.jeurceramsoc.2017.11.051.

[80] J.P. Lafon, E. Champion, D. Bernache-Assollant, Processing of AB-type carbonated hydroxyapatite Ca10−x(PO4)6−x(CO3)x(OH)2−x−2y(CO3)y ceramics with controlled composition, J. Eur. Ceram. Soc. 28 (1) (Jan. 2008) 139–147, https://doi.org/10.1016/j.jeurceramsoc.2007.06.009.

[81] Y. Chen, X. Miao, Thermal and chemical stability of fluorohydroxyapatite ceramics with different fluorine contents, Biomaterials 26 (11) (2005) 1205–1210, https://doi.org/10.1016/j.biomaterials.2004.04.027.

[82] Y. Guo, J. Guan, J. Yang, Y. Wang, C. Zhang, Q. Ke, Hybrid nanostructured hydroxyapatite–chitosan composite scaffold: bioinspired fabrication, mechanical properties and biological properties, J. Mater. Chem. B 3 (2015) 4679–4689, https://doi.org/10.1039/c5tb00175g.

[83] M. Ibrahim, A.A. Mahmoud, O. Osman, A. Refaat, E.S.M. El-Sayed, Molecular spectroscopic analysis of nano-chitosan blend as biosensor, Spectrochim. Acta, Part A 77 (4) (2010) 802–806, https://doi.org/10.1016/j.saa.2010.08.007.

[84] G. Lawrie, et al., Interactions between alginate and chitosan biopolymers characterized using FTIR and XPS, Biomacromolecules 8 (8) (2007) 2533–2541, https://doi.org/10.1021/bm070014y.

[85] A. Rogina, M. Ivanković, H. Ivanković, Preparation and characterization of nano-hydroxyapatite within chitosan matrix, Mater. Sci. Eng. C 33 (8) (2013) 4539–4544, https://doi.org/10.1016/j.msec.2013.07.008.

[86] J. Li, D. Zhu, J. Yin, Y. Liu, F. Yao, K. Yao, Formation of nano-hydroxyapatite crystal in situ in chitosan-pectin polyelectrolyte complex network, Mater. Sci. Eng. C 30 (6) (2010) 795–803, https://doi.org/10.1016/j.msec.2010.03.011.

[87] Z. Ansari, et al., In-Situ synthesis and characterization of chitosan/hydroxyapatite nanocomposite coatings to improve the bioactive properties of Ti6Al4V substrates, Materials 13 (17) (Aug. 2020) 3772, https://doi.org/10.3390/ma13173772.

[88] A. Ressler, et al., Osteogenic differentiation of human mesenchymal stem cells on substituted calcium phosphate/chitosan composite scaffold, Carbohydr. Polym. 277 (August 2021) 2022, https://doi.org/10.1016/j.carbpol.2021.118883.

[89] C. Piccirillo, R.C. Pullar, E. Costa, A. Santos-Silva, M.M.E. Pintado, P.M.L. Castro, Hydroxyapatite-based materials of marine origin: a bioactivity and sintering study, Mater. Sci. Eng. C 51 (2015) 309–315, https://doi.org/10.1016/j.msec.2015.03.020.

[90] I. Reis Lavagnini, J.V. Campos, A.G. Storion, A.O. Lobo, R. Raj, E. Maria de Jesus Agnolon Pallone, Influence of flash sintering on phase transformation and conductivity of hydroxyapatite, Ceram. Int. 47 (7) (2021) 9125–9131, https://doi.org/10.1016/j.ceramint.2020.12.036.

[91] M. Haug, F. Bouville, C. Ruiz-Agudo, J. Avaro, D. Gebauer, A.R. Studart, Cold densification and sintering of nanovaterite by pressing with water, J. Eur. Ceram. Soc. 40 (3) (2020) 893–900, https://doi.org/10.1016/j.jeurceramsoc.2019.10.034.

[92] F. Bouville, A.R. Studart, Geologically-inspired strong bulk ceramics made with water at room temperature, Nat. Commun. 8 (1) (Mar. 2017), 14655, https://doi.org/10.1038/ncomms14655.

[93] A. Ndayishimiye, et al., Roadmap for densification in cold sintering: chemical pathways, Open Ceram 2 (July) (2020), 100019, https://doi.org/10.1016/j.oceram.2020.100019.

[94] E.F. Morgan, G.U. Unnikrisnan, A.I. Hussein, Bone mechanical properties in healthy and diseased states, Annu. Rev. Biomed. Eng. 20 (1) (Jun. 2018) 119–143, https://doi.org/10.1146/annurev-bioeng-062117-121139.

[95] F. Liu, J. Zhang, P. Liu, Q. Deng, D. He, Strengthening of alumina ceramics under cold compression, Ceram. Int. 46 (3) (Feb. 2020) 3984–3988, https://doi.org/10.1016/j.ceramint.2019.09.257.

[96] J. Guo, S.S. Berbano, H. Guo, A.L. Baker, M.T. Lanagan, C.A. Randall, Cold sintering process of composites: bridging the processing temperature gap of ceramic and polymer materials, Adv. Funct. Mater. 26 (39) (2016) 7115–7121, https://doi.org/10.1002/adfm.201602489.

[97] J. Guo, et al., Cold sintering: a paradigm shift for processing and integration of ceramics, Angew. Chem. Int. Ed. 55 (38) (2016) 11457–11461, https://doi.org/10.1002/anie.201605443.

[98] A.J. Ruys, M. Wei, C.C. Sorrell, M.R. Dickson, A. Brandwood, B.K. Milthorpe, Sintering effects on the strength of hydroxyapatite, Biomaterials 16 (5) (1995) 409–415, https://doi.org/10.1016/0142-9612(95)98859-C.

[99] S. Pramanik, A.K. Agarwal, K.N. Rai, A. Garg, Development of high strength hydroxyapatite by solid-state-sintering process, Ceram. Int. 33 (3) (Apr. 2007) 419–426, https://doi.org/10.1016/j.ceramint.2005.10.025.

[100] L. Feng, M. Chittenden, J. Schirer, M. Dickinson, I. Jasiuk, Mechanical properties of porcine femoral cortical bone measured by nanoindentation, J. Biomech. 45 (10) (2012) 1775–1782, https://doi.org/10.1016/j.jbiomech.2012.05.001.

[101] A. Ibrahim, N. Magliulo, J. Groben, A. Padilla, F. Akbik, Z. Abdel Hamid, Hardness, an important indicator of bone quality, and the role of collagen in bone hardness, J. Funct. Biomater. 11 (85) (Dec. 2020) 1–10, https://doi.org/10.3390/jfb11040085.

[102] M.L. Lau, K.T. Lau, H. Ku, F. Cardona, J.H. Lee, Analysis of heat-treated bovine cortical bone by thermal gravimetric and nanoindentation, Compos. B Eng. 55 (2013) 447–452, https://doi.org/10.1016/j.compositesb.2013.06.027.

[103] X. Wang, X. Chen, P. Hodgson, C. Wen, Elastic modulus and hardness of cortical and trabecular bovine bone measured by nanoindentation, Trans. Nonferrous Metals Soc. China 16 (Jun. 2006) s744, https://doi.org/10.1016/S1003-6326(06)60293-8. –s748.

[104] P.K. Zysset, X. Edward Guo, C. Edward Hoffler, K.E. Moore, S.A. Goldstein, Elastic modulus and hardness of cortical and trabecular bone lamellae measured by nanoindentation in the human femur, J. Biomech. 32 (10) (Oct. 1999) 1005–1012, https://doi.org/10.1016/S0021-9290(99)00111-6.

[105] W. wei Wu, et al., Bone hardness of different anatomical regions of human radius and its impact on the pullout strength of screws, Orthop. Surg. 11 (2) (2019) 270–276, https://doi.org/10.1111/os.12436.

[106] P. Jongwattanapisan, et al., In vitro study of the SBF and osteoblast-like cells on hydroxyapatite/chitosan–silica nanocomposite, Mater. Sci. Eng. C 31 (2) (Mar. 2011) 290–299, https://doi.org/10.1016/j.msec.2010.09.009.

[107] Y.W. Gu, K.A. Khor, P. Cheang, Bone-like apatite layer formation on hydroxyapatite prepared by spark plasma sintering (SPS), Biomaterials 25 (18) (Aug. 2004) 4127–4134, https://doi.org/10.1016/j.biomaterials.2003.11.030.

[108] J. Cao, R. Lian, X. Jiang, X. Liu, Formation of porous apatite layer after immersion in SBF of fluorine-hydroxyapatite coatings by pulsed laser deposition improved in vitro cell proliferation, ACS Appl. Bio Mater. 3 (6) (Jun. 2020) 3698–3706, https://doi.org/10.1021/acsabm.0c00328.

[109] F. Baino, S. Yamaguchi, The use of simulated body fluid (SBF) for assessing materials bioactivity in the context of tissue engineering: review and challenges, Biomimetics 5 (Oct. 2020) 1–19, https://doi.org/10.3390/biomimetics5040057.

[110] Y.W. Gu, K.A. Khor, P. Cheang, In vitro studies of plasma-sprayed hydroxyapatite/Ti-6Al-4V composite coatings in simulated body fluid (SBF),

Biomaterials 24 (9) (2003) 1603–1611, https://doi.org/10.1016/S0142-9612(02)00573-2.

[111] S. Kobayashi, T. Murakoshi, Characterization of mechanical properties and bioactivity of hydroxyapatite/β-tricalcium phosphate composites, Adv. Compos. Mater. 23 (2) (2013) 163–177, https://doi.org/10.1080/09243046.2013.844897.

[112] A.J. Salgado, O.P. Coutinho, R.L. Reis, Bone tissue engineering: state of the art and future trends, Macromol. Biosci. 4 (8) (2004) 743–765, https://doi.org/10.1002/mabi.200400026.

[113] S. Bose, M. Roy, A. Bandyopadhyay, Recent advances in bone tissue engineering scaffolds, Trends Biotechnol. 30 (10) (Oct. 2012) 546–554, https://doi.org/10.1016/j.tibtech.2012.07.005.